

## Document Version

Final published version

## Licence

CC BY

## Citation (APA)

Hu, X., Martin, H. A., Poelma, R., Huang, J., van Rijckevorsel, H., Scholten, H., Smits, E., van Driel, W. D., & Zhang, G. (2024). Exploring the process-microstructure-thermal properties relationship of resin-reinforced Ag sintering material for high-power applications via 3D FIB-SEM nanotomography. *Materials and Design*, 244, Article 113185. <https://doi.org/10.1016/j.matdes.2024.113185>

## Important note

To cite this publication, please use the final published version (if applicable).  
Please check the document version above.

## Copyright

In case the licence states "Dutch Copyright Act (Article 25fa)", this publication was made available Green Open Access via the TU Delft Institutional Repository pursuant to Dutch Copyright Act (Article 25fa, the Taverne amendment). This provision does not affect copyright ownership.  
Unless copyright is transferred by contract or statute, it remains with the copyright holder.

## Sharing and reuse

Other than for strictly personal use, it is not permitted to download, forward or distribute the text or part of it, without the consent of the author(s) and/or copyright holder(s), unless the work is under an open content license such as Creative Commons.

## Takedown policy

Please contact us and provide details if you believe this document breaches copyrights.  
We will remove access to the work immediately and investigate your claim.



# Exploring the process-microstructure-thermal properties relationship of resin-reinforced Ag sintering material for high-power applications via 3D FIB-SEM nanotomography

Xiao Hu <sup>a,b,\*</sup>, Henry Antony Martin <sup>a,c</sup>, René Poelma <sup>d,\*\*</sup>, Jianlin Huang <sup>b</sup>, Hans van Rijckevorsel <sup>b</sup>, Huib Scholten <sup>b</sup>, Edsger Smits <sup>c</sup>, Willem D. van Driel <sup>a</sup>, Guoqi Zhang <sup>a,\*\*</sup>

<sup>a</sup> Delft University of Technology, Department of Microelectronics, Mekelweg 4, Delft, 2628CD, the Netherlands

<sup>b</sup> Ampleon B.V., Halfgeleiderweg 8, Nijmegen, 6534AV, the Netherlands

<sup>c</sup> Chip Integration Technology Center, Transistorweg 5T, Nijmegen, 6534AT, the Netherlands

<sup>d</sup> Nexperia, Jonkerbosplein 52, Nijmegen, 6534AB, the Netherlands

## ARTICLE INFO

### Keywords:

3D FIB-SEM nanotomography  
Geometric tortuosity  
Effective thermal conductivity  
Transient thermal impedance  
Thermal percolation phenomenon  
High-power application

## ABSTRACT

Resin-reinforced Ag sintering materials represent a promising solution for die-attach applications in high-power devices requiring enhanced reliability and heat dissipation. However, the presence of resin and intricate microstructure poses challenges to its thermal performance, and improvement strategies remain unclear. This work utilizes 3D FIB-SEM nanotomography to reconstruct the microstructure of this material under various process conditions. The analysis reveals that, even with an Ag volume fraction as low as 47.3%, Ag particles form a robust 3D network. Geometric tortuosity quantifies the effect of different sintering conditions on the Ag particle network in all spatial directions. Effective thermal conductivity is simulated based on realistic microstructure models. Results show a significant negative correlation between tortuosity and effective thermal conductivity. Increasing sintering temperature in Model B notably reduces tortuosity and enhances effective thermal conductivity. Sensitivity analysis underscores the dominant role of Ag volume fraction in regulating effective thermal conductivity. Finally, transient thermal impedance measurement of this material as a thin die-attach layer in actual high-power devices demonstrated its application potential. This article strives to explore the relationship between process, microstructure, and thermal properties of this material to provide a reference for further development.

## 1. Introduction

With the rapid development of power electronics technology toward higher power density and miniaturization, devices face more severe thermal performance and reliability challenges. Recognizing the significance of enhancing the thermal and electrical conductivity, the industry is transitioning from Gold-tin and Pd-based solder alloy (with a thermal conductivity of 57 W/m·k) to Silver (Ag) and Copper (Cu) based sintering materials. This transition has notably elevated the thermal conductivity of die-attach materials to over 100 W/m·k, rendering them more suitable for high-power applications [1–4]. However, the inherent hardness of traditional sintering materials, ranging approximately from 80 to

130 GPa, exposes them to susceptibility regarding thermo-mechanical stresses, which may lead to potential adhesive and cohesive fractures [5,6]. In response, many novelty composite die-attach materials have emerged to trade-off between thermal and mechanical properties, such as SiC-reinforced, Graphene-reinforced, thermoplastic resin-reinforced Ag sintering materials, even Ag-Cu foam sheets, etc., [7–10].

The resin-reinforced Ag sintering material is one of the new composites where thermoplastic resins are added to the metal paste to occupy the porous regions, thereby tuning the mechanical properties of the material [11,12]. Nonetheless, the advent of thermoplastic resins has made the thermal properties of this material challenging to determine due to the sensitivity of many parameters related to composition and process

\* Corresponding author at: Delft University of Technology, Department of Microelectronics, Mekelweg 4, Delft, 2628CD, the Netherlands.

\*\* Corresponding authors.

E-mail addresses: [x.hu-1@tudelft.nl](mailto:x.hu-1@tudelft.nl) (X. Hu), [rene.poelma@nexperia.com](mailto:rene.poelma@nexperia.com) (R. Poelma), [g.q.zhang@tudelft.nl](mailto:g.q.zhang@tudelft.nl) (G. Zhang).

<https://doi.org/10.1016/j.matdes.2024.113185>

Received 4 March 2024; Received in revised form 18 June 2024; Accepted 23 July 2024

Available online 2 August 2024

0264-1275/© 2024 The Author(s). Published by Elsevier Ltd. This is an open access article under the CC BY license (<http://creativecommons.org/licenses/by/4.0/>).

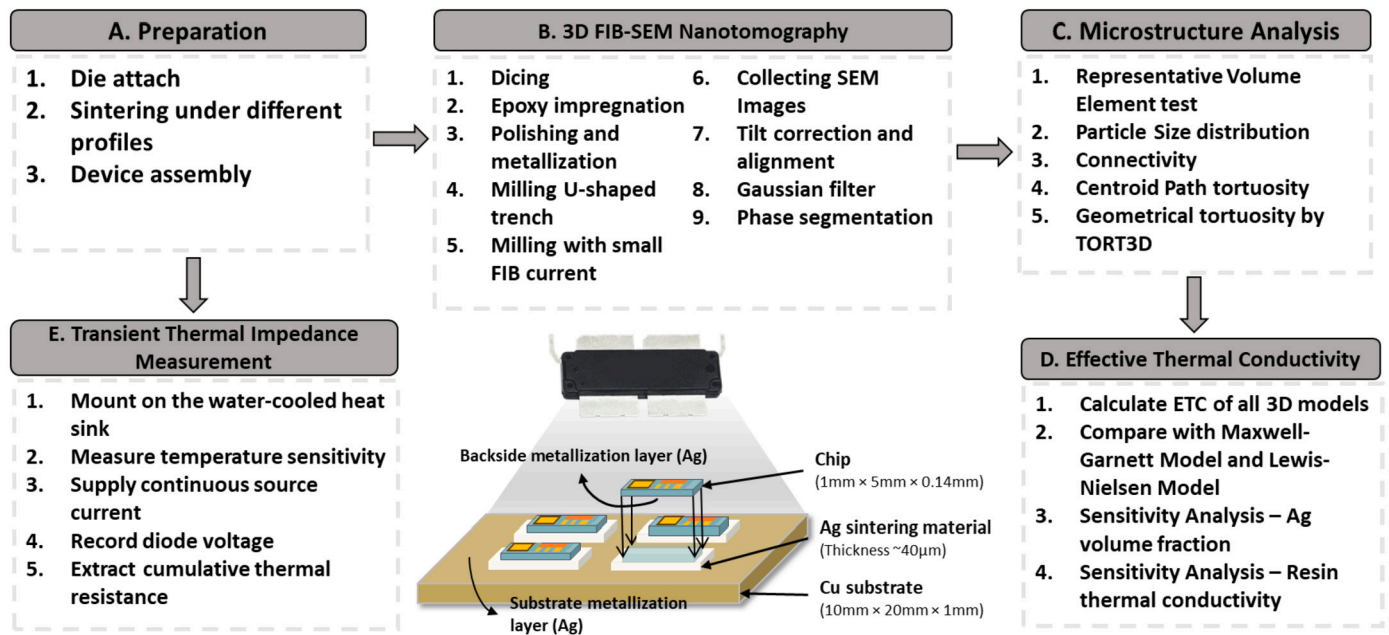


Fig. 1. The framework of this study and the schematic of the device structure.

conditions. Furthermore, the method to evaluate the effective thermal conductivity (ETC) of composites at the micro-nano scale remains elusive. The lack of clarity in understanding the regulatory mechanism of ETC makes it difficult to carry out the next step of material development and device-level applications.

The dilemma in estimating the ETC of this composite material arises from the complexity of its microstructure and a remarkable phenomenon, thermal percolation. The microstructure is composed of resins and a mixture of nano- and micron-sized Ag particles with irregular shapes, as shown in Fig. 2, and it can be found that Ag particles appear dispersed in the cross-sectional image. However, as the Ag volume fraction approaches the percolation threshold, there exists the potential for the formation of a three-dimensional (3D) network. The percolation threshold is the critical point at which the dispersed phase (in this case, Ag) forms interconnected pathways within the matrix (in this case, the resin), and this geometric transition can lead to nonlinear enhancements in properties such as electrical conductivity and thermal conductivity [13–15]. The difficulty of choosing a method to estimate thermal properties mainly comes from two factors. One is that the traditional effective medium theoretical model based on the assumption of uniform field and low concentration (40%) will fail at higher volume fractions [16,17]. Second, conventional strategies, treating the particles as regular shapes or obtaining ETC from the 2D cross-sectional images of the Ag paste, are only suitable for high Ag volume fraction (> 80%) and are insufficient to describe the contribution of the 3D Ag particle network to ETC when the Ag volume fraction is lower [18–21].

Advanced characterization techniques play a pivotal role in unraveling the complexity of microstructure. Among these techniques, the 3D Focused Ion Beam Scanning Electron Microscopy (FIB-SEM) Nanotomography emerges as a powerful tool, offering unprecedented insights into the 3D nanoscale morphology, connectivity, and geometric tortuosity of the microstructure [22–24]. This technique is higher resolution than micro-CT and is less time-consuming and cheaper than 3D X-ray and the tomography techniques based on Electron Backscatter Diffraction (EBSD) and Transmission Electron Microscopy (TEM) [25–27]. The novelty of this work is to obtain continuous microstructural slices of resin-reinforced Ag sintering materials directly from the die-attach layer of functional RF devices, reconstructing the Ag particle connection network with a resolution of about 50 nm. At this fine resolution, we have achieved for the first time the discriminative analysis of the differences

in material microstructure under different process conditions, while providing a reliable and realistic 3D model for simulation.

Clarifying the regulatory mechanism of the ETC will help to optimize the thermal properties. As acknowledged, the ETC of composites is intricately influenced by process and the sizes, shapes, volume fractions, and even topologies of composition [28]. Here, we use the Porous Microstructure Analysis (PuMA) with the support of a high-performance cluster to perform the ETC calculation of 3D realistic microstructural models over 430 million voxels [29]. This approach facilitates a nuanced exploration of the impact of various Ag volume fractions while providing insights into the impact of selecting resins with different thermal conductivities as the matrix on ETC.

Exploring the practical application potential of this material as a thin die attach layer has the challenge of measuring thermal performance at the micro/nano-scale. [30,31]. Conventional steady-state measurements are common techniques for measuring the thermal properties of bulk materials [32,33]. For transient thermal measurement, the Laser Flash method can measure the thermal conductivity of bulk materials with a thickness of ~1 mm [34]. The  $3\omega$  method can be used for the thin film of ~10 μm, but it needs to prepare samples, and wire and sheet metal require evaporation [35]. However, the thickness of the die attach layer is usually 100 μm. In this case, we chose the transient dual interface test method to perform transient thermal impedance measurements in actual devices to demonstrate its application potential [36,37].

Overall, we strive to achieve a comprehensive understanding of the intricate relationships linking the processing, microstructure, and thermal performance of this material [38–41]. The process involves the integration of 3D FIB-SEM nanotomography, quantitative microstructure analysis, numerical simulation, and device-level measurement. The framework was shown in Fig. 1. The Methodology section documents the preparation process of the samples, the steps involved in utilizing FIB-SEM and 3D modeling, and the subsequent methods of geometric tortuosity calculation and transient thermal impedance measurements. Microstructure analysis, ETC calculation results, and transient thermal resistance measurements are discussed in Section 3, Results and Discussion. These insights contribute to the fundamental understanding of this material's microstructure and thermal performance and pave the way for the design and optimization of advanced materials for high-power electronic packaging.

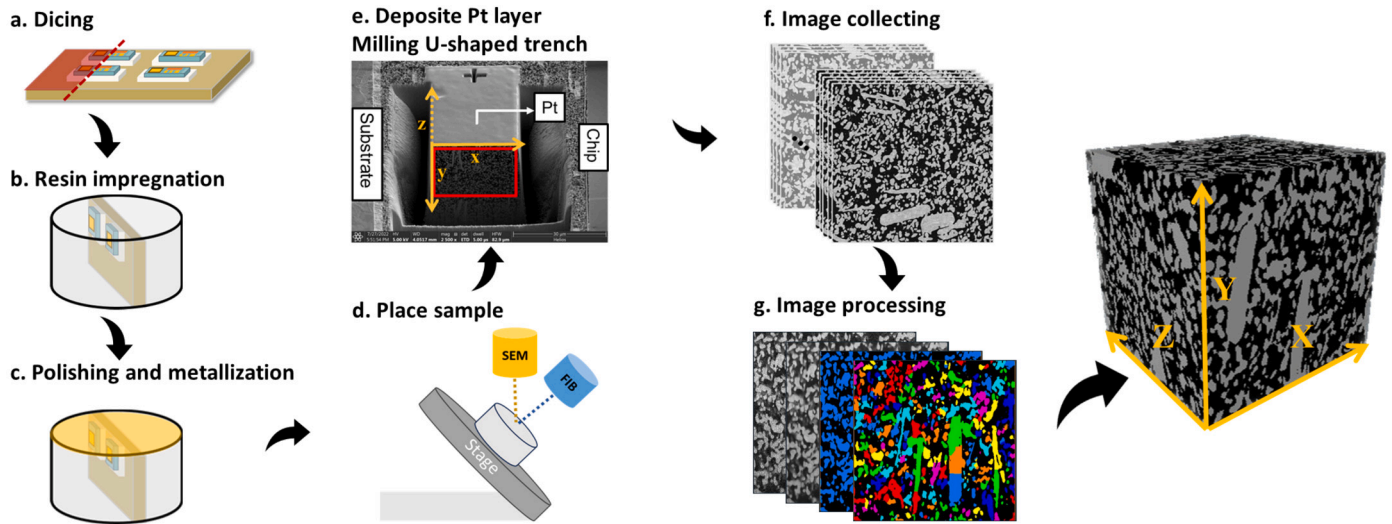


Fig. 2. The workflow of FIB-SEM 3D nanotomography on the resin-reinforced Ag sintering layer.

## 2. Methodology

### 2.1. Samples preparation

The devices in the sample are Silicon-based Laterally Diffused Metal Oxide Semiconductor (LDMOS) high-power RF devices. The chips were sintered to the Cu substrate using resin-reinforced Ag sintering material. The complete stack is wire-bonded and assembled in Over-molded Plastic (OMP) packages. The schematic of the device's exterior and interior is shown in Fig. 1. There are three different sintering profiles to analyze the influence of sintering conditions: (i.) Sintering 2 hours under 200 °C, (ii.) sintering 2 hours under 250 °C and (iii.) sintering 4 hours under 200 °C. The Bond-Line Thicknesses of Ag sintering layer is about 60  $\mu\text{m} \pm 10 \mu\text{m}$ . All sintering procedures are pressureless processes within air ambient.

### 2.2. FIB milling

The workflow shown in Fig. 2 was followed to reconstruct the microstructure of the sintered Ag layer. In the preparation stage, the devices with the OMP package were diced and potted with epoxy resin, like step (a) and (b). In step (e), the surface of the samples was ground and polished, and ion milling was used for surface cleaning. Since the Ag sintering layer contains resin, a 20 nm thick gold layer is sputtered on the sample's surface for better conductivity and stable imaging quality. After that, the sample was sent into the vacuum chamber of FIB-SEM, like step (d). A FIB-SEM system named Helios G4 CX from FEI was used for SEM image stack collection. Under the view of SEM, as shown in step (e), the Region of Interest (ROI) was chosen, and a Platinum (Pt) protective layer of 1  $\mu\text{m}$  was deposited on xz plane using an ion source. A wide and deep U-shaped trench was milled around the ROI using the maximum FIB current of 21 nA. The distance between inter-slices ( $\Delta z$ ) was established through the utilization of a reference mark positioned on the upper section of the Pt layer. To mitigate the risk of overlooking minuscule Ag particles, the determined inter-slice distance has been set at 50 nm. Next, the FIB milling was performed with an ion beam current of 2.5 nA at 30kV. Finally, we collected more than 500 continuous SEM images for all samples. These images have been done tilt correction in the Y direction due to the SEM imaging being realized at an angle of 52°. The automatic FIB milling process was implemented with the help of Auto Slice & View 4 Software [42].

### 2.3. 3D reconstruction and analyzing

For image processing, the tilt of SEM images was corrected for alignment, and a Gaussian filter was chosen to enhance the SEM image. The phase segmentation of the Ag and the resin was implemented based on gray-scale thresholding. Finally, the rendered images were stitched together as a 3D model. Here, the actual length of each voxel along the x-axis, y-axis, and z-axis is 19.64 nm, 19.64 nm, and 50 nm, respectively. To understand the connected network of Ag particles, The Separate module and the Generate Pore Network Model module in AVIZO, a materials characterization software, are used to identify the particle volume size and connectivity [43].

To compare and verify, two methods were used to obtain the geometrical tortuosity that characterizes the morphological properties. First, the Centroid Path Tortuosity module (CPM) in AVIZO calculated the centroid path tortuosity, a type of tortuosity calculated by tracking the center of mass of each phase on each slice and comparing the length of this path to the straight path in the same [44]. In addition, another type of geometric tortuosity factor is calculated by a Matlab code based skeleton shortest-path search method (SSPSM) called TORT3D [45,46]. This method first extracts the skeleton of Ag particles from the binary image and then applies Dijkstra's algorithm to the skeleton to identify the shortest path. The skeleton is formed by the medial axis of the Ag particle network, which simplifies the path search task and largely retains the topological and geometric characteristics of the Ag particle network. TORT3D will mark the start point of all possible paths and search their shortest paths, finally, geometric tortuosity,  $\tau_g$ , is defined as  $\tau_g = \frac{\langle L_g \rangle}{L_s}$ ,  $\langle L_g \rangle$  is the average length of all paths through the Ag particles network.  $L_s$  is the straight-line length for each axis. The schematic diagram of the TORT3D processing process is shown in Fig. 3.

### 2.4. Transient thermal impedance measurement method

Here, we chose the transient dual interface test method, a standardized procedure outlined by JEDEC51-14 for characterizing semiconductor devices' thermal performance, i.e., to determine the Junction-to-Case thermal resistance [36,37]. The semiconductor device's Temperature Sensitive Electrical Parameters (TSEP) enable measuring the device junction temperature by translating the electrical output to temperature readings. The Junction-to-Ambient transient thermal impedance of the devices in the OMP package was determined by measuring the device junction temperature, and then the thermal performance of the material was analyzed at the device level. Similar experiments for thermal

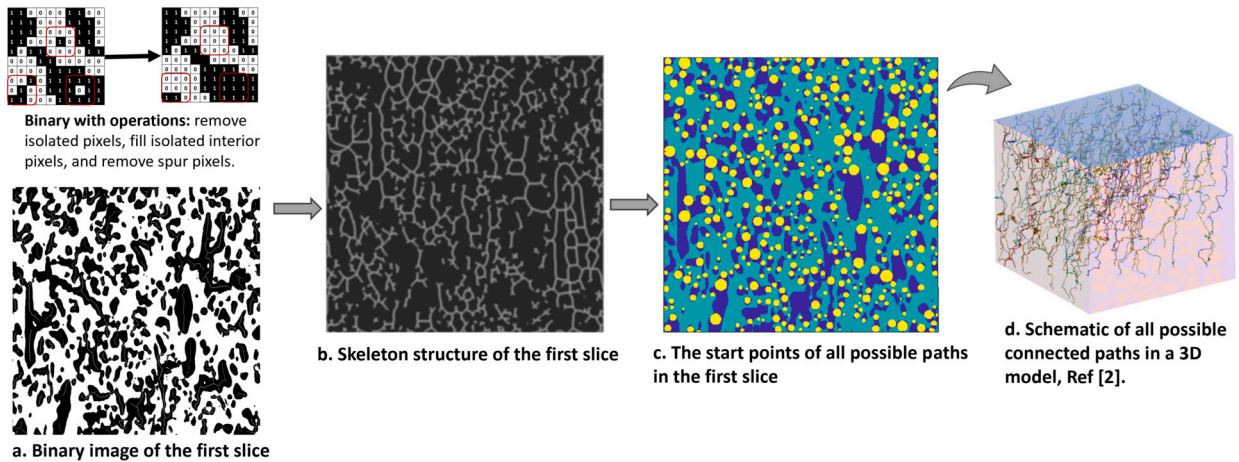


**Fig. 3.** Schematic of the image processing in TORT3D. (a). Obtained the binary image of the SEM image and optimized it with operations like removing and filling isolated pixels. Here, the black area is Ag, and the white area is resin. (b). Obtained the skeleton structure of the Ag particle network from the binary image. (c). Determined the start points of all possible paths based on the skeleton structure. Here, the blue area is Ag, and the green area is resin. (d). Run TORT3D to mark and record all possible connected paths to calculate  $\tau_g$ .

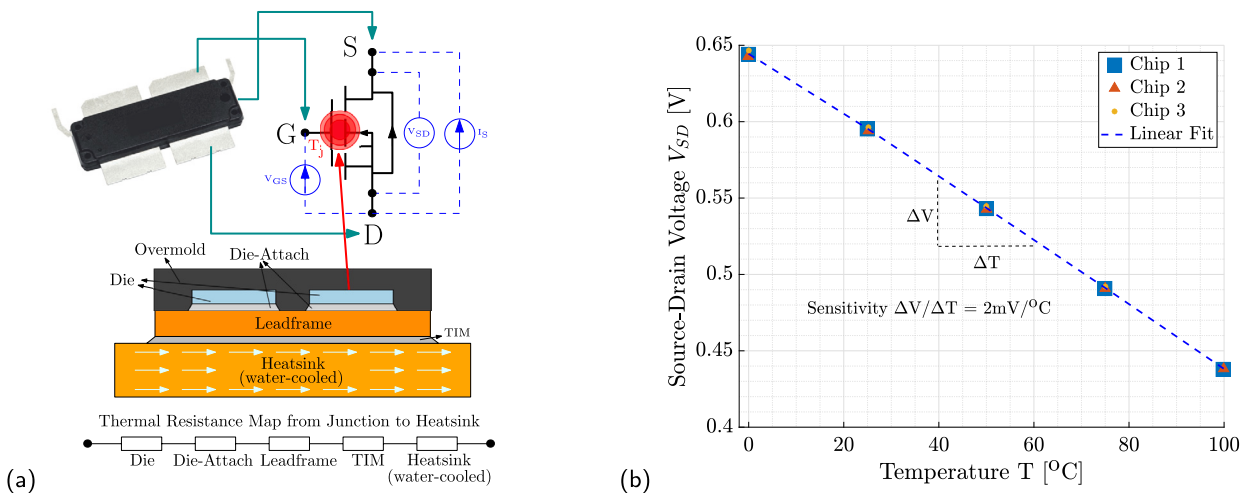


**Fig. 4.** (a). A schematic of an OMP package mounted on a water-cooled heatsink is shown, and different layers within the package are highlighted. The sourcing and measuring points are indicated in blue. (b). The voltage drop across the body diode ( $V_{SD}$ ) was measured at five different temperatures between 0°C to 100°C, to identify the temperature sensitivity.

resistance evaluation of Pb solders, Pb-free solders, and Ag sintering materials have been studied in [47–50].

First, the high-power RF device with an over-molded package was electrically connected with 4-point kelvin contacts for accurate measurements. A schematic of the OMP package mounted on a water-cooled heat sink is shown in Fig. 4(a), along with an electrical layout of the LDMOS device. The LDMOS is a voltage-controlled device (i.e.,) the device is forward biased when a positive voltage is applied between the gate-source (+  $V_{GS}$ ) and drain-source (+  $V_{DS}$ ) terminals, reverse biased when the gate is closed ( $V_{GS} = 0$ ) and a negative voltage is applied between the drain-source terminal ( $-V_{DS} = V_{SD}$ ). When reverse-biased the device operates through the intrinsic body diode (a PN junction formed between the source-drain terminals) which has a higher sensitivity to temperature. The temperature sensitivity of the body diode voltage ( $V_{SD}$ ) was measured at five different temperatures between 0°C to 100°C and shown in Fig. 4(b). Then, a continuous source current  $I_S$  of 3A was supplied through the body diode for 100 seconds, and the resultant change in the diode voltage  $V_{SD}$  was measured at a sampling rate of  $\sim 15 \mu s$  per data point. The device was measured with and without Thermal Interface Material (TIM) by mounting it on a water-cooled heat sink. The water temperature is recorded, and the device tempera-

ture is measured, which enables extracting the junction-to-case thermal resistance of the package. The measurement results are shown in the subsequent results and discussion section.

### 3. Results and discussions

#### 3.1. Microstructure analysis

##### 3.1.1. Representative volume element test

Three 3D models were generated for different sintering conditions based on the FIB-SEM nanotomography, as shown in Fig. 5. They are **Model A** - 2 hours at 200 °C, **Model B** - 2 hours at 250 °C and **Model C** - 4 hours at 200 °C. The actual side length of these models is about 17  $\mu m$  (875 voxels  $\times$  19.64 nm in the x/y-axis, 340 voxels  $\times$  50 nm in the z-axis). Through naked eye observation, it is only clear that the number of tiny particles in model B is less than in the other two models, and it is still difficult to distinguish differences in the microstructure of all models, such as the Ag volume fraction ( $VF_{Ag}$ ) and particle size.

The Representative Volume Element (RVE) represents a fundamental unit within a material that includes its essential structure and properties, thus allowing the representation and simulation of material behavior

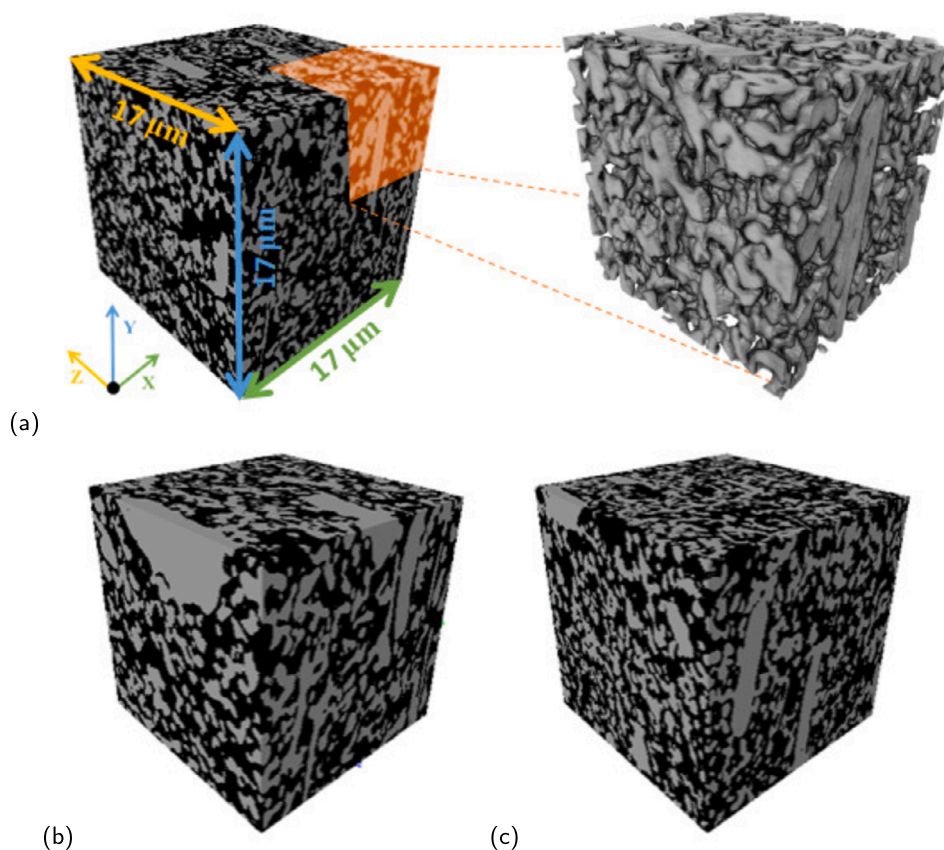


**Fig. 5.** (a) Model A (2 hours at 200 °C) and its One-eight Ag particles network. (b) Model B (2 hours at 250 °C). (c) Model C (4 hours at 200 °C). The black area is the resin, and the gray area is Ag. Models A, B and C all have a side length of 17 μm.

at larger scales. The role of RVE becomes more critical when studying composite materials in this work, as we want to consider as many microstructural features as possible, whether they are irregular or rod-shaped particles. Here, the initial 3D model was set up as a cube with a side length of 6 μm. The side length is gradually expanded to 20 μm, and the volume fraction of Ag is measured simultaneously. As shown in Fig. 6 (a), when the total volume gradually increased, the  $VF_{Ag}$  of all three models was observed to be stable at 46.2%, 47.0%, 45.0%, respectively. In Fig. 6(b), the  $VF_{Ag}$  of more than 400 FIB slices in each model were counted, and the slice size is  $17 \mu\text{m} \times \mu\text{m}$ . Although the Ag area fraction in each slice varied, the final average area fraction of each model was 46.12%, 47.30%, and 45.38%, respectively, which were close to the results of 3D models. The final models' total volume in Fig. 5 are  $4924.57 \mu\text{m}^3$ , and these models are reasonable RVEs.

The difference in  $VF_{Ag}$  corresponding to different sintering conditions is within 2%. Based on this result, it is difficult to determine whether different process conditions cause this difference or whether the distribution of Ag particles is uneven. Moreover, the  $VF_{Ag}$  in the three models is less than 50%, which may mean that the ETC of this material is not ideal like other Ag sintering materials with high  $VF_{Ag}$  reported in Ref. [51]. In the next section, the connectivity and size distribution of the Ag particles in all models are examined to understand whether possible Ag connect networks exist and the influence of sintering conditions on these.

### 3.1.2. Particle size distribution and connectivity

Microstructure contains a wealth of invaluable information, including the distribution of Ag particle size and the connectivity among these particles. To identify the interconnecting network of Ag particles, the 26-neighbor-connectivity criterion (6 faces, 12 edges, or eight vertexes), 18-neighbor-connectivity criterion (6 faces, 12 edges), and 6-neighbor-connectivity criterion (6 faces) were defined for the connec-

tion between voxels [44]. The results indicated that the connectivity of the Ag particles was above 99% for all three models so that those seemingly separated particles in 2D cross-sectional SEM images were interconnected within a 3D space. Fig. 7 shows isolated Ag particles that are not connected to the main Ag particles network in three microstructural models.

Subsequently, we investigate the particle volume and area distribution obtained by separating the connected Ag particles. The Separate Module-based Chamfer-Conservative method in Avizo is used to separate Ag particles for all models, and the particle volume size distribution diagram is shown in Fig. 8. The particle size distribution of model A and model C are nearly identical. Still, comparing that of model A and model B, it can be found that the number of particles less than  $1 \mu\text{m}^3$  is greatly reduced, and the number of particles with the size from 1 to  $2 \mu\text{m}^3$  is increased. According to Fig. 8(d)(e)(f), which are the zoom-in images at 0 to  $1.8 \mu\text{m}$  range of Fig. 8(a)(b)(c), we can obviously found that the sintering at 250 °C makes the tiny particles (volume less than  $0.2 \mu\text{m}^3$ ) fuse with the large particles more, and the extension of sintering time at 200 °C makes the tiny particles form more particles with volume of 0.2 to  $0.4 \mu\text{m}^3$ . The effect of temperature increase on sintering coarsening is also limited by particle size.

To compare, the area size of dispersed Ag particles in 2D SEM images with a side dimension of  $30 \mu\text{m}$  were counted using Image J, and the particle area size distribution diagram is shown in Fig. 9. By comparing Fig. 9(a) and (b), increasing the sintering temperature from 200 °C to 250 °C increased the area of dispersed Ag particles, and the number of particles in large areas increased significantly. Comparing Fig. 9(a) and (c), it can be found that when the sintering temperature is kept at 200 °C, only extending the sintering time has limited promotion to the formation of larger particles, and the particle distribution trend is almost the same. Here, we obtain consequences consistent with the particle volume distribution analysis, but our discussion is based on dispersed

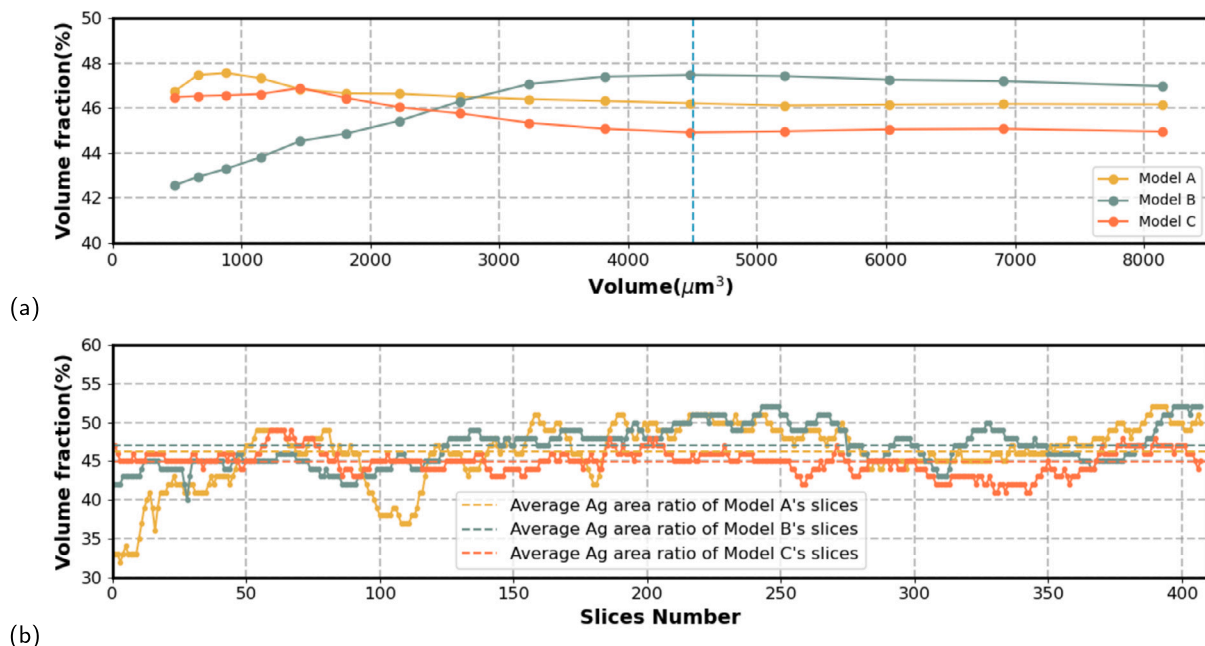


Fig. 6. (a) Representative Volume Element test results for all 3D models. (b) The Ag volume fraction of more than 400 FIB slices in each model.

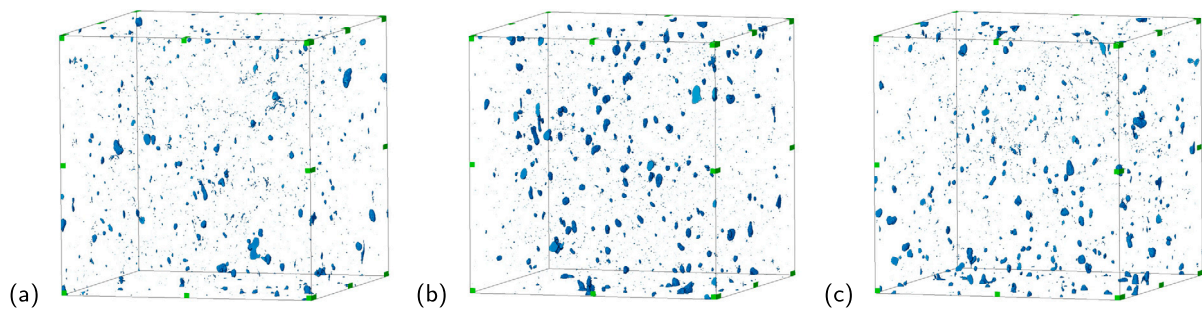


Fig. 7. Isolated Ag particles in (a) Model A (2 hours at 200 °C). (b) Model B (2 hours at 250 °C). (c) Model C (4 hours at 200 °C).

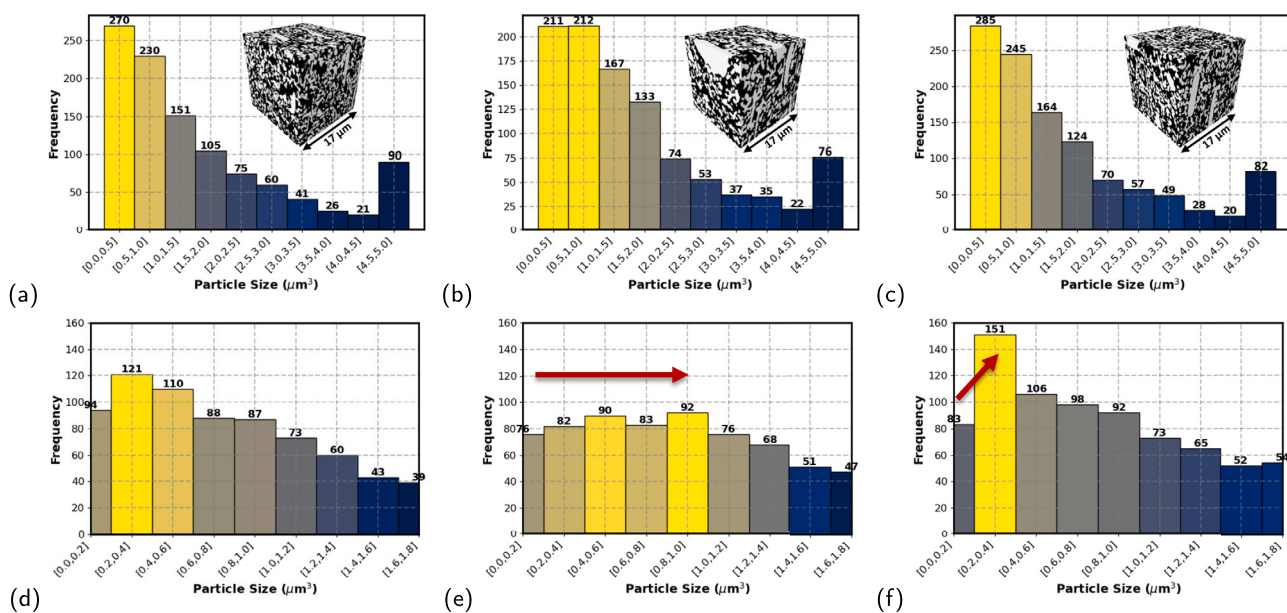


Fig. 8. The particle volume distribution and its zoom-in at 0 to 1.8  $\mu\text{m}^3$  range of Model A (2 hours at 200 °C) (a)(d), that of Model B (2 hours at 250 °C) (b)(e), and that of Model C (4 hours at 200 °C) (c)(f).

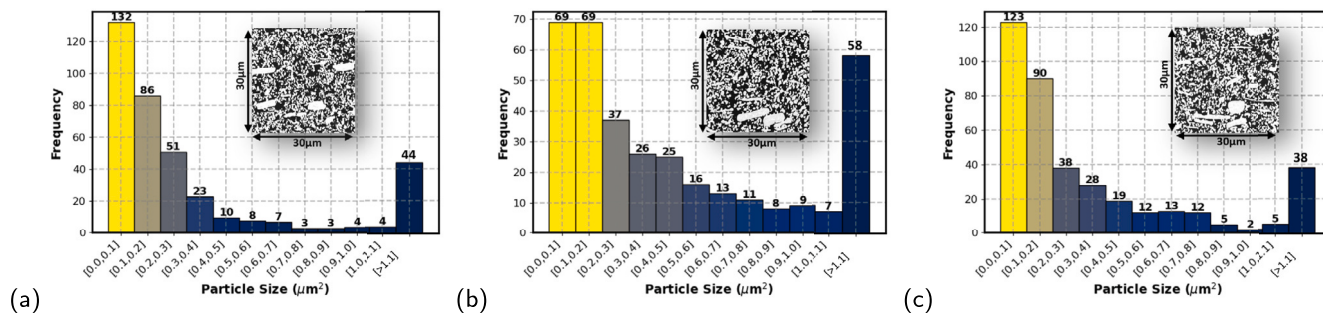


Fig. 9. (a) The particle area distribution in a 2D SEM image of the sample sintered at 200 °C for 2 hours, (b) at 250 °C for 2 hours, and (c) at 200 °C for 4 hours.

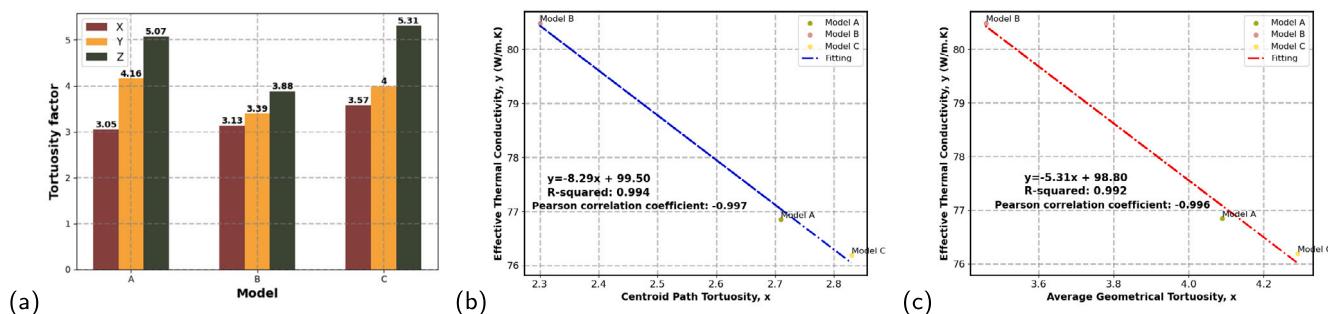


Fig. 10. (a) Calculated tortuosity factors by using TORT3D along X/Y/Z axes for all models. (b) Relationship between Centroid Path Tortuosity (x) and Effective Thermal Conductivity (y). (c) Relationship between Average Geometrical Tortuosity (x) and Effective Thermal Conductivity (y).

Table 1

The physical dimensions, the total volume, the fraction of Ag and Resin volume, and the Ag particles' connectivity under different voxel neighbor-connectivity criteria for all models.

	Model A	Model B	Model C
3D Reconstruction Size (X × Y × Z) (μm)	17.02*17.02*17.00	17.02*17.02*17.00	17.02*17.02*17.00
Total Volume (μm <sup>3</sup> )	4924.57	4924.57	4924.57
Ag Volume Fraction (%)	46.12	47.30	45.38
Resin Volume Fraction (%)	53.88	52.7	54.62
26-Neighbor Connectivity (%)	99.88	99.73	99.82
18-Neighbor Connectivity (%)	99.86	99.73	99.81
6-Neighbor Connectivity (%)	99.85	99.70	99.79
Centroid Path Tortuosity	2.71	2.30	2.83
Geometrical Tortuosity (X/Y/Z)	3.05/4.16/5.07	3.13/3.39/3.88	3.57/4.00/5.31

particles in 2D slices and does not involve the influence of sintering conditions on the Ag particle network.

### 3.1.3. Geometrical tortuosity factors

In the study of porous materials, tortuosity contributes to a deep understanding of transport processes in porous media by calculating the degree of bending of the flux motion path in porous media with respect to the straight path [44]. In this work, to avoid introducing time-consuming physical diffusion simulations in such complex microstructures, geometric tortuosity is employed to understand the microstructure and quantify the impact of sintering conditions on the Ag particles network.

For Model A, B, and C, their centroid path tortuosity obtained by tracking the Ag area's centroid of each slice is 2.71, 2.30, and 2.80, respectively. This implies that in the slice direction (z-axis), the Ag particle network in Model B has the lowest tortuosity, and the network is denser. However, due to simple implementation, the centroid path tortuosity is limited in the distance globally, omitting the local variations in the structure, such as can arise from bottlenecks and discontinuities. Therefore, we further used TORT3D based on SSPSM to obtain the geometric tortuosity in order to reflect more topological and geometric features of the Ag particle network.

As shown in Fig. 10(a), the tortuosity of three models along the X/Y/Z direction shows different degrees of anisotropy, but they all follow  $\tau_z > \tau_y > \tau_x$ , which may be an inherent feature of the microstructure of this material. The highest tortuosity along the z-axis might result from the fact that the actual length of a voxel (19.64 nm × 19.64 nm × 50 nm) is longer in the z-axis than in the x/y axis. In other words, the image sampling density is low in the z-direction. Notably, Model B exhibits tortuosity values within 4.00 in all directions, and the difference between the maximum and minimum values is 0.75. Compared with the obvious differences between the other two models, the Ag particles network in Model B has shorter transport paths along all directions. It is consistent with the centroid tortuosity result.

All microstructure findings are summarized in Table 1. The results indicate that all the aforementioned sintering conditions can achieve 99% connectivity of Ag particles, though the volume fraction of Ag is lower than 50%. Particle size distribution and geometrical tortuosity results based on 3D FIB-SEM nanotomography quantified the different sintering degrees of Ag particles under different sintering conditions. Extending the sintering time at 200 °C has a limited effect on the coarsening of Ag particles. It only promotes the combination of tiny particles (volume less than 0.2 μm<sup>3</sup>) into larger tiny particles (0.2 to 0.4 μm<sup>3</sup>). In particular, in Model B, during the two-hour sintering at 250 °C, tiny

Ag particles are more combined with larger particles, obviously reducing the tortuosity of the Ag particles network along the y-axis and z-axis and making this network more compact. Obtaining geometric tortuosity based on digital microstructures is more intuitive, cost-effective, and friendly to larger systems than physical tortuosity. In future work, the phenomenological relationship between geometric tortuosity and physical tortuosity can still be established through correlation analysis.

### 3.2. From microstructure to thermal behaviors

To bridge the results of the microstructure analysis to the thermal performance, ETC calculations of this material and transient thermal impedance measurements in the actual device are performed in the following.

#### 3.2.1. Calculate effective thermal conductivity

In this work, the finite volume solver in PuMA performs the ETC calculation of three microstructure models. First, PuMA discriminant voxel according to the gray threshold for Ag or resin then generates a thermal conductivity matrix to store the conductivity values for each phase. Here, the thermal conductivity of Ag is set to 429 W/(m·K), and that of resin is 0.5 W/(m·K). For each simulation, a temperature gradient field along the x-axis is forced and converged to a steady state, and the x-axis is the direction of heat dissipation from Die to Substrate in the actual device. The boundary condition in the non-simulation direction is set as periodic. The iterative solver we used is the Conjugate Gradients iterative method, and the tolerance is set as  $10^{-4}$ . Despite performed RVE test, each 3D model still has approximately 430 million voxels, so the calculation was implemented on DelftBlue, a high-performance computer cluster at Delft University of Technology [52]. According to the thermal percolation theory, when the thermal conductivity of the filler particles is much higher than that of the matrix, it can be assumed that most of the heat will be transferred through the particle chains. Since Ag particles have high connectivity and their thermal conductivity is much higher than that of the resin, the interfacial thermal resistance between Ag and resin is not considered here.

With these settings, the ETC of Models A, B, and C are 76.85, 80.48, and 76.19 W/(m·K), respectively. Combined with the previous tortuosity results, the relationship between microstructure and ETC can be further analyzed. Fig. 10(b) depicts the relationship between centroid path tortuosity (x) and ETC (y). A linear regression fit yields the equation  $y = -8.29x + 99.50$  with an  $R^2$  value of 0.994, indicating a strong negative correlation between centroid path tortuosity and ETC. The Pearson correlation coefficient is -0.997, further confirming the high degree of correlation. Fig. 10(c) shows the relationship between average geometrical tortuosity (x), which is the average geometric tortuosity of all directions of a model, and ETC (y). The linear regression fit, in this case, results in the equation  $y = -5.31x + 98.80$  with an  $R^2$  value of 0.992. Similar to the previous figure, this indicates a strong negative correlation, supported by a Pearson correlation coefficient of -0.996.

Overall, these figures suggest that both centroid path tortuosity and average geometrical tortuosity exhibit a significant negative correlation with ETC. As the tortuosity decreases, the ETC increases. This finding is crucial for revealing the influence of process conditions on the microstructure and can be used to quickly judge the thermal conductivity by geometric features, thus guiding the optimization of the thermal properties of this material.

For comparison, traditional empirical models such as the Maxwell-Garnett (MG) model and the Lewis-Nielsen (LN) model were used to calculate the ETC at different  $VF_{Ag}$ s. The thermal conductivity of Ag and resin was the same as the setting in PuMA. These models do not consider any effects related to the interface between the resin and Ag. Furthermore, the material is treated as isotropic in these models. Maxwell-Garnett Model:

$$K_{eff} = k_1 \frac{2k_1 + k_m - 2\phi_m(k_1 - k_m)}{2k_1 + k_m + \phi_m(k_1 - k_m)} \quad (1)$$

Lewis-Nielsen model:

$$K_{eff} = \frac{1 + AB\phi}{1 - B\psi\phi}, \quad (2)$$

where,

$$B = \left( \frac{k_1/k_m - 1}{k_1/k_m + A} \right), \quad (3)$$

$$\psi = 1 + \left( \frac{1 - \phi_m}{\phi_m^2} \right). \quad (4)$$

Here,  $K_{eff}$  is ETC,  $k_m$  is the thermal conductivity of the matrix, and  $k_1$  is the thermal conductivity of the dispersed phase.  $\phi$  and  $\phi_m$  are the volume fraction of the dispersed phase and matrix, respectively. In the Lewis-Nielsen model, the particle shape is considered the sphere, and distribution factor A is set as 1.58, meaning randomly [28].

In the zoom-in area of Fig. 12(a), we can find the ETC results of the MG model and LN model are both lower than 5 W/(m·K) when the volume fraction of Ag lower than 50%. As mentioned previously, these models are clearly unsuitable for describing thermal conductivity changes in thermal percolation phenomena because they are based on assumptions of uniform fields or low concentrations. Although compared with other models, the Lewis-Nielsen model already takes into account the influence of particle shape and dispersed phase connection network. For the material involved in thermal percolation phenomena, simulation based on 3D digital microstructure models represents the promising direction.

Here, Model B is selected as the study case due to it having a relatively close geometric tortuosity in all directions. Additionally, it is further assumed to be isotropic so that it can be compared with the MG and LN models. The  $VF_{Ag}$  in Model B changes from 10% to 80% by adjusting the gray value during threshold segmentation, as shown in Fig. 11. In Fig. 11(a), the rod-shape and flake Ag particles still exist after reducing the  $VF_{Ag}$ . The blue line in Fig. 12(a) shows the ETC of the model with different VFs when the  $T_{resin}$  is set to 0.5 W/(m·K). Obviously, the nonlinear enhancement of ETC already occurs when the  $VF_{Ag}$  is quite low, so we can't define the thermal percolation threshold by the ETC enhancement from linear to nonlinear as mentioned in Ref. [13].

In Fig. 12(b), the connectivity of the Ag particle network under different volume fractions based 6-neighbor-connectivity criterion is calculated. When VF is only 10.27%, the connectivity of the Ag particle network is as high as 83.81%. This means that at quite low  $VF_{Ag}$ , the Ag particles network still was configured by rod-shape or flake Ag particles with only a small amount of Ag dispersed. In the following section, we delve into examining the influence of  $VF_{Ag}$ s variation and different resin thermal conductivities ( $T_{resin}$ ) on the ETC.

#### 3.2.2. Sensitivity analysis

Generally, the thermal conductivity range of resin materials is relatively low, typically between 0.1 and 0.5 W/(m·K). That's because of the long chainlike structures and gaps in the polymer molecular structure, resulting in the obstruction of heat transfer. And, this is the reason many thermal management materials are skeptical about the ETC of resin-reinforced composites. In this material, we have to make a trade-off between reliability and thermal performance by adding or reducing resin. Therefore, it is essential to study the ETC of this material under different  $VF_{Ag}$ s and different resin matrices with different thermal conductivity.

We implemented the sensitivity analysis to examine the impact of variations in  $VF_{Ag}$  and  $T_{resin}$  on ETC. The resin's thermal conductivity was assumed to change from 0.1 to 10 W/(m·K) on a logarithmic scale. All ETC results under different  $T_{resin}$  and different VFs are shown in Fig. 13(a). The reference configuration is  $T_{resin0} = 0.5$  m·K and  $VF_0 = 47.3\%$ . Fig. 13(b) illustrates the ETC changes ( $\Delta T_{eff}/T_{eff0}$ ) caused by the variation in the resin thermal conductivity ( $\Delta T_{resin}/T_{resin0}$ ) under different  $VF_{Ag}$ s. Fig. 13(c) shows the ETC changes caused by the variation in  $VF_{Ag}$ s ( $\Delta VF_{Ag}/VF_0$ ) when choosing different resin thermal

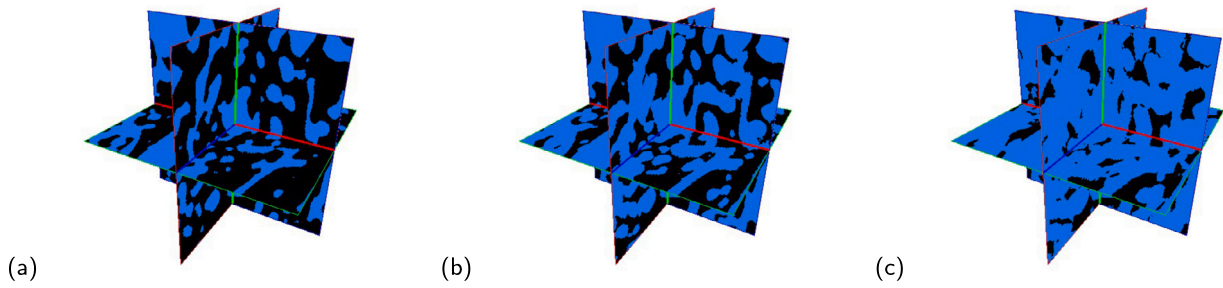


Fig. 11. Adjusting the gray value during threshold segmentation to change the Ag volume fraction to (a) 40.10%, (b) 60.20%, (c) 80.16%.

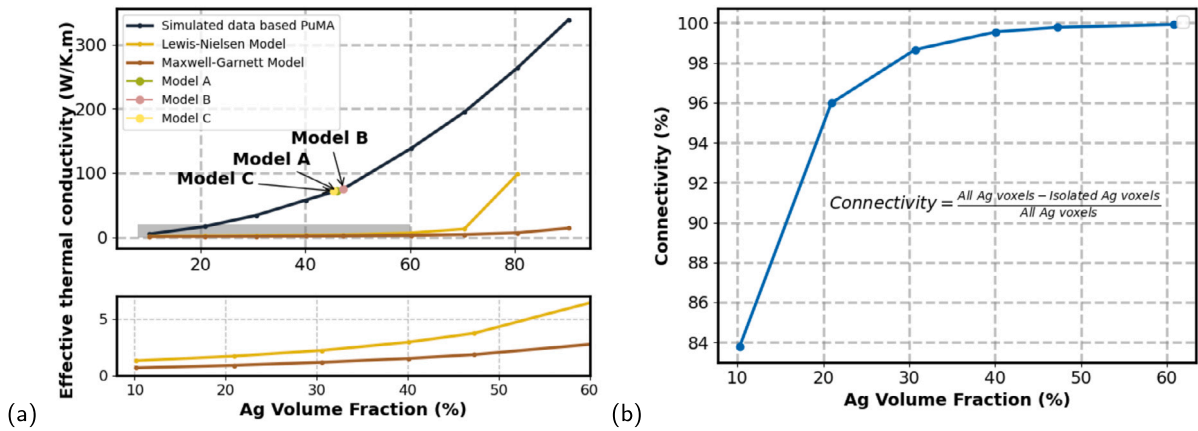


Fig. 12. (a) Effect of Ag volume fraction on ETC, and the comparison of ETC results with other models. (b) The connectivity variation of Ag particles network under different Ag volume fractions.

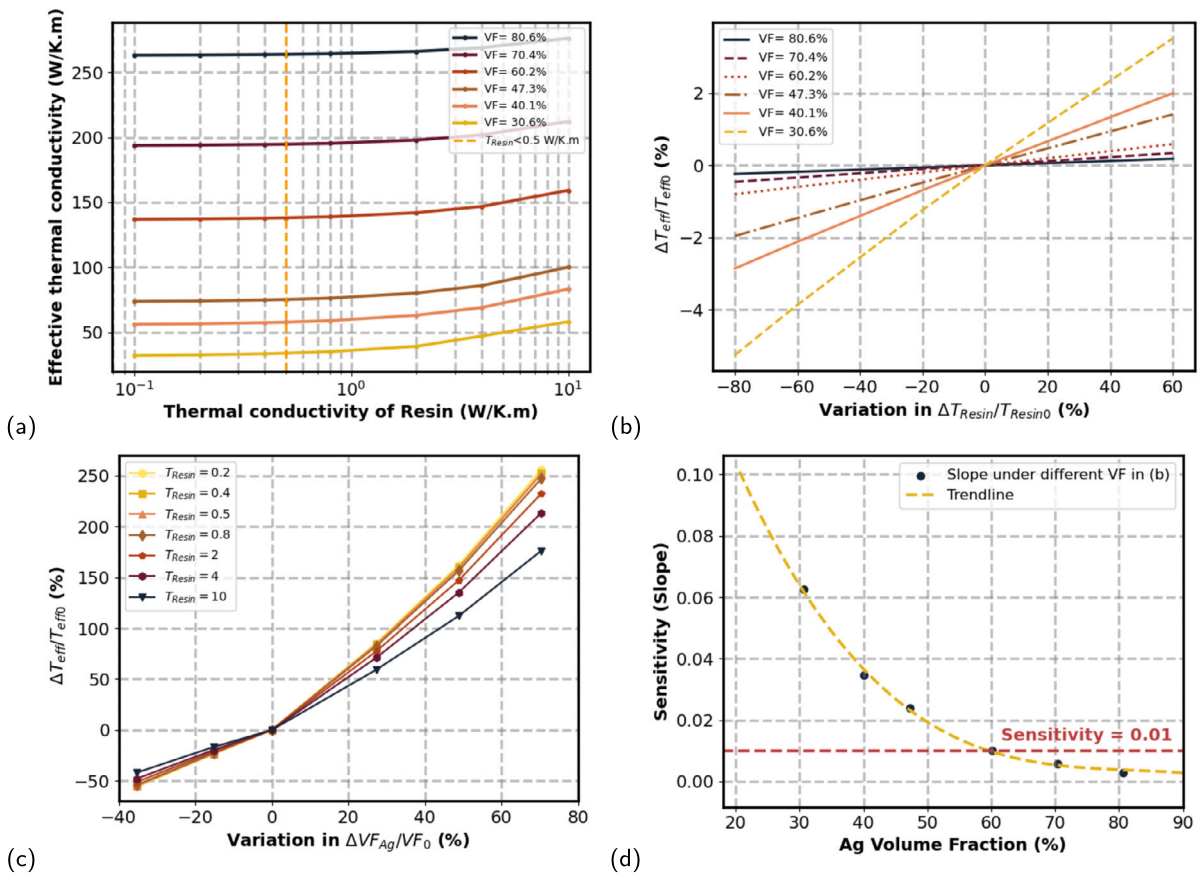
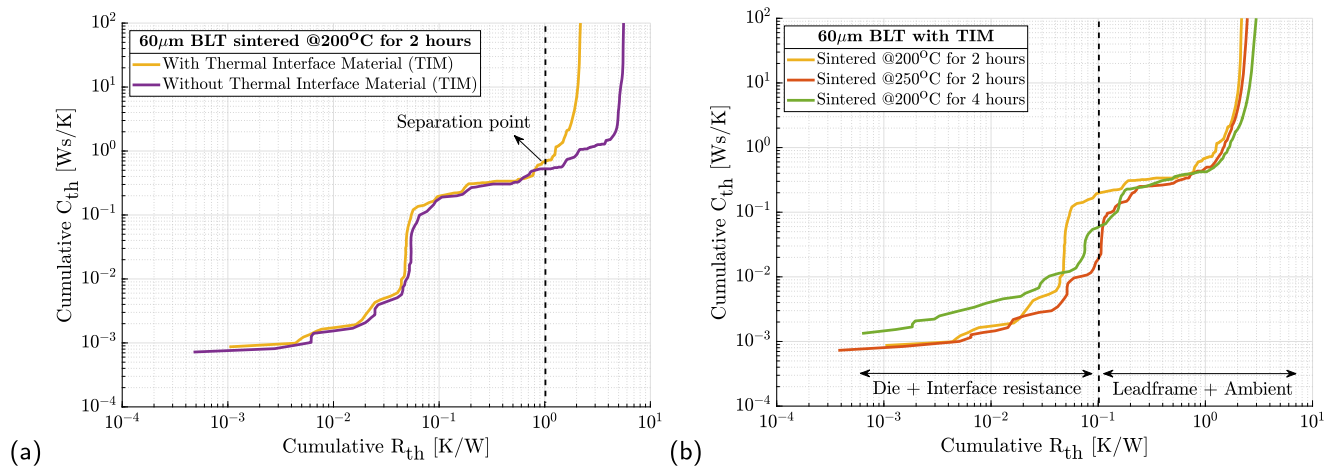


Fig. 13. (a) Effect of resin's Thermal Conductivity on ETC. Sensitivity analysis about the effect of (b) resin's thermal conductivity and (c) Ag volume fraction. (d) The sensitivity variation for different resin's thermal conductivity to volume fraction.



**Fig. 14.** (a). The Junction-to-Case package thermal resistance was extracted by measuring the device mounted onto a water-cooled heat sink with and without a thermal interface material to identify the separation point as highlighted. (b). Packages with diverse sintering conditions exhibit no significant differences. The subtle changes observed between packages processed at different sintering conditions are negligibly small to be considered a variation due to different sintering conditions.

conductivities. Comparing the variation range of ETC in Fig. 13(b) and (c), we can see that ETC is greatly affected by the change of  $VF_{Ag}$ . When the  $T_{resin}$  is increased by 20%, the increases of ETC under different  $VF_{Ag}$ s are all within 2%. However, when  $VF_{Ag}$  is increased by 20%, ETC under different  $T_{resin}$ s all mostly increased by about 50%.

The slope of ETC change in Fig. 13(b), caused by different resin thermal conductivity changes, is regarded as the sensitivity. For example, when the  $VF_{Ag}$  is 30.6%, the sensitivity is 0.063. Fig. 13(d) describes the change of sensitivity with  $VF_{Ag}$ s. With increasing  $VF_{Ag}$ , the sensitivity sharply decreases, and when the  $VF_{Ag}$  is 80%, the sensitivity is almost close to 0. This is also consistent with the results of Sasaki et al., when  $VF_{Ag}$  is 85%, the remaining 15% is pores or filled with resin, which has little effect on materials' thermal conductivity [11,12]. These results provide a reference, at a volume fraction of 60%, the change of resin thermal conductivity has no obvious effect on the ETC of this material (sensitivity  $\leq 0.01$ ), and the calculated ETC is also higher than 136 W/(m·K). This result, combined with other factors, such as the mechanical stiffness and plasticity of the material at different  $VF_{Ag}$ s, can help determine the optimal volume fraction.

### 3.2.3. Transient thermal impedance measurement results

Fig. 14(a) indicates the separation point (when measured with and without a thermal interface material), indicating the junction-to-case package thermal resistance. The experimental results are plotted on a logarithmic scale to visualize the interface thermal resistance contribution. The interface thermal resistance, in this context, encompasses the cumulative impact of various resistances, including the backside metal resistance of the die, the die-attach material resistance, the metalization resistance on the lead frame, and the contact resistances. Hence, packages with different sintering conditions (temperature and time) were further measured with thermal interface materials and the experimental findings are shown in Fig. 14(b).

In all three samples subjected to varying sintering conditions, the aggregate resistance (die and interface) remained less than  $\sim 0.1$  K/W, which initially meets the application requirement by comparing with Ref [66–68]. However, no significant measurable differences were observed between different sintering conditions. The subtle variations observed among the diverse sintering conditions are negligibly small, possibly due to the inherent variability among individual devices and not necessarily due to different sintering conditions. This implies that the conventional method of determining the junction-to-case package thermal resistance method outlined by JESD51-14 may not be sensitive enough to detect variations from diverse sintering conditions on extremely thin interfaces ( $\sim 60$   $\mu\text{m}$ ). Further research is required to

improve the transient thermal impedance measurement resolution by estimating the delta transient  $\Delta Z_{th}(t, \Delta x)$  with  $\Delta x$  indicating the die-attach thickness. This can be achieved by using two thermally sensitive devices interfaced using the die-attach material, thereby the cumulative resistance-capacitance network would indicate changes due to different process conditions and different thicknesses.

Hence, it can be inferred that the 3D FIB-SEM nanotomography used in this study is effective and important for comprehending the influence of varying sintering conditions on the thermal behavior of extremely thin interfaces.

### 3.3. Discussion

The experimental thermal conductivity and shear strength ranges of traditional solder alloy, metal-based pastes, and new reinforced or doped metal-based pastes used for die-attach materials are summarized in Table 2. Due to variations in measurement methods and the influence of sample dimensions, direct comparison of thermal conductivity values across these materials is challenging. Nevertheless, it can still be found that the thermal conductivity of the material with a high resin volume fraction (50%) is still better than that of traditional solders like Au-based and Sn-based solder alloy, and the material with a lower resin volume fraction (15%) has thermal property close to that of Ag hybrid pastes. Reinforced materials, such as those doped with 1 wt% AlN or reinforced with 0.25 wt% Graphene, achieve shear strengths exceeding 50 MPa. Notably, from Table 2, it shows that the Ag volume fraction of these reinforced materials is mostly keeper than 90%, which means the researchers are still conservative about how much Ag volume to replace the mechanical properties they want to achieve.

This work aims to provide a control strategy of  $VF_{Ag}$  based on thermal properties to inspire the development of new composite sintering materials. 3D FIB-SEM Nanotomography presents the characteristics of the microstructure and thermal properties, indicating that the highly connected Ag network can still provide a thermal conductivity of 80.48 W/(m·K) when the  $VF_{Ag}$  is only 47.3%. At the same time, it is also pointed out that under the highly connected Ag network, when the thermal conductivity of Ag is much higher than the thermal conductivity of the resin, there is no need to consider the influence of interfacial thermal resistance. When the Ag volume fraction is higher than 60%, the thermal conductivity of the filled resin has little effect on the ETC of the material. Reducing the Ag volume fraction can not only be used to replace the desired mechanical properties but is also an important means of reducing costs.

**Table 2**  
Thermal conductivity and shear strength at room temperature of die attach materials for high-power application.

Type	Name	Thermal Conductivity (W/m.K)	Shear Strength @RT (MPa)	Ref.
Solder Alloy	Au-based	27-59	130	[3]
	Sn-based Pb-free	20-66	28-64	[4,53]
	Sn-based Pb-bearing	23-53	8-28	[4,54]
	Zn-based	77-110	60-100	[55,56]
Metal Paste	Ag nanopaste	200-240	20-80	[3,51,57]
	Ag hybrid paste	166-265	15-49	[58]
	Ag micropaste	80-220	20-40	[59,60]
	Cu nanopaste	-	65-115	[61,69]
	Cu micropaste	94	9-17	[62]
	Ag-Cu nanopaste	159	70-80	[4,63]
Reinforced	20 wt% Si-doped	-	35	[64]
	1 wt% AlN-doped	-	54	[65]
	5 wt% SiC-reinforced	35	46	[7]
	0.25 wt% Graphene-reinforced	200	55	[10]
	15 wt% Resin-reinforced	186	35	[11,12]
	90 at% Ag-Cu foam sheet	-	28-41	[8,9]
	50 %wt Resin-reinforced	80	-	This work

#### 4. Conclusion

Using 3D FIB-SEM nanotomography, we reconstructed the microstructure of resin-reinforced Ag sintering material under different sintering times and temperatures at the nanoscale. After quantitatively analyzing the microstructural and thermal properties, some insights were obtained:

a. 3D FIB-SEM nanotomography accurately identified microstructural differences during pressureless sintering at different temperatures and times. Microstructure analysis quantified these differences by obtaining geometric tortuosity and particle size distribution. Increasing the temperature from 200 to 250 °C promotes Ag particles coarsen, thus reducing the tortuosity. However, extending the sintering time from 2 to 4 hours at 200 °C shows no significant structural changes.

b. Using high-performance cluster computing, ETC simulations based on 3D realistic microstructural models were implemented. The Ag particles network's connectivity in the 3D microstructural model revealed a robust network formation and made ETC reach 80.48 W/(m·K), despite the  $VF_{Ag}$  being just at 47.3%. The ETC of Models A, B, and C are 76.85, 80.48, and 76.19 W/(m·K), respectively.

c. Both the centroid path tortuosity and the average geometric tortuosity are significantly negatively correlated with ETC. Increasing the sintering temperature enables Model B to obtain the lowest tortuosity and the highest ETC among the three models. This analysis helps to optimize the pressureless sintering process to obtain better ETC.

d. Sensitivity analyses revealed that the regulatory mechanism of ETC is dominated by the  $VF_{Ag}$ , where the influence of resin thermal conductivity can even become negligible under a high  $VF_{Ag}$ . For instance, when  $VF_{Ag}$  is 60%, the sensitivity is lower than 0.01. Combining the material's mechanical properties in future work will help determine the optimal volume fraction during material development.

e. Transient thermal impedance measurements indicated that the thermal resistance of this material, when applied to an actual high-power RF device, is less than 0.1 K/W. The influences of unknown factors such as bond line thickness and contact resistance on the measurement results are also pointed out, and improvement strategies are provided.

In future work, to provide a specific material optimization solution, we will introduce mechanical properties and reliability tests such as thermal storage or cycling to fully evaluate the performance of this material. Methodologically, although 3D FIB-SEM nanotomography is shown as a powerful solution to investigate complex microstructure, it is still limited to long slicing and modeling time for the industry. Future improvements include exploring the feasibility of generating a full 3D reconstruction of resin-reinforced Ag sintering material using microstructural parameters obtained from a single 2D cross-sectional SEM

image. Leverage advanced characterization and simulation technologies to accelerate new material development for the advanced packaging of high-power semiconductor devices.

#### CRedit authorship contribution statement

**Xiao Hu:** Writing – original draft, Visualization, Methodology, Investigation. **Henry Antony Martin:** Writing – original draft, Visualization, Methodology. **René Poelma:** Writing – review & editing, Supervision. **Jianlin Huang:** Writing – review & editing, Supervision. **Hans van Rijckevorsel:** Resources. **Huib Scholten:** Resources. **Edsger Smits:** Supervision, Resources. **Willem D. van Driel:** Writing – review & editing, Supervision, Resources. **Guoqi Zhang:** Supervision, Resources, Funding acquisition.

#### Declaration of competing interest

The authors declare that they have no known competing financial interests or personal relationships that could have appeared to influence the work reported in this paper.

#### Data availability

Data will be made available on request.

#### Acknowledgement

Thanks to Hozanna Miro and Dustin Laur from the Kavli Nanolab Delft for knowledge support about FIB, and Dong Hu from the ECTM group of TU Delft for helping with FIB training. Also, thanks to Ampleon B.V. for the sample preparation. This publication is part of the Fundamentals of Backside Metals System project for 5G RF Power Modules, financed by the Dutch Research Council (NWO) under project No. 17969.

#### References

- [1] C. Buttay, D. Planson, B. Allard, D. Bergogne, P. Bevilacqua, C. Joubert, M. Lazar, C. Martin, H. Morel, D. Tournier, C. Raynaud, State of the art of high temperature power electronics, in: *Microtechnology and Thermal Problems in Electronics*, Mater. Sci. Eng., B 176 (4) (2011) 283–288.
- [2] A.A. Bajwa, Y. Qin, R. Reiner, R. Quay, J. Wilde, Assembly and packaging technologies for high-temperature and high-power GaN devices, *IEEE Trans. Compon. Packag. Manuf. Technol.* 5 (10) (2015) 1402–1416.
- [3] H. Zhang, J. Minter, N.-C. Lee, A brief review on high-temperature, Pb-free die-attach materials, *J. Electron. Mater.* 48 (1) (2019) 201–210, <https://doi.org/10.1007/s11664-018-6707-6>.

- [4] K.S. Tan, Y.H. Wong, K.Y. Cheong, Thermal characteristic of sintered Ag-Cu nanopaste for high-temperature die-attach application, *Int. J. Therm. Sci.* 87 (2015) 169–177, <https://doi.org/10.1016/j.ijthermalsci.2014.08.022>, <https://www.sciencedirect.com/science/article/pii/S1290072914002488>.
- [5] W. Liu, A. Rong, C. Wang, Z. Zheng, Y. Tian, R. Xu, Z. Wang, Recent progress in rapid sintering of nanosilver for electronics applications, *Micromachines* 9 (2018) 346.
- [6] K.S. Siow (Ed.), *Die-Attach Materials for High Temperature Applications in Micro-electronics Packaging: Materials, Processes, Equipment, and Reliability*, Springer International Publishing, Cham, 2019.
- [7] X. Long, Z. Li, X. Lu, H. Guo, C. Chang, Q. Zhang, A. Zehri, W. Ke, Y. Yao, L. Ye, J. Liu, Mechanical behaviour of sintered silver nanoparticles reinforced by SiC microparticles, *Mater. Sci. Eng. A* 744 (2019) 406–414, <https://doi.org/10.1016/j.msea.2018.12.015>, <https://www.sciencedirect.com/science/article/pii/S0921509318316940>.
- [8] H. Zhang, H. Zhang, Q. Jia, C. Yin, Z. Deng, W. Guo, Z. Wan, Novel SiC-based power device bonding materials of nano foam sheet and its characteristic and properties, in: *IEEE Transactions on Components, Packaging and Manufacturing Technology*, IEEE Trans. Compon. Packag. Manuf. Technol. 13 (6) (2023) 897–905, <https://doi.org/10.1109/TCPMT.2023.3288389>, <https://ieeexplore.ieee.org/document/10159137>.
- [9] C. Yin, K. Wumaeraili, Y. Zhang, Y. Wu, J. Zhang, W. Guo, Y. Zhu, X. Song, Q. Jia, H. Zhang, Novel Ag-Cu foam sheet with multi-layer composite structure for high performance joining of SiC power chips, *Mater. Charact.* 209 (2024) 113696, <https://doi.org/10.1016/j.matchar.2024.113696>, <https://www.sciencedirect.com/science/article/pii/S1044580324000767>.
- [10] H. Zhang, S. He, G. Qu, Z. Deng, G. Zou, Q. Jia, E. Deng, W. Guo, Improved thermal conductivity and reliability through graphene reinforced nanopaste for power devices in new energy vehicles, in: *IEEE Transactions on Components, Packaging and Manufacturing Technology*, IEEE Trans. Compon. Packag. Manuf. Technol. 14 (1) (2024) 52–60, <https://doi.org/10.1109/TCPMT.2023.3339686>, <https://ieeexplore.ieee.org/document/10348599>.
- [11] K. Sasaki, N. Mizumura, A. Tsuno, S. Yagci, G. Kopp, Development of low-temperature sintering nano-silver die attach materials for bare cu application, in: *2017 21st European Microelectronics and Packaging Conference (EMPC) & Exhibition*, 2017, pp. 1–5.
- [12] N. Mizumura, K. Sasaki, Development of low-temperature sintered nano-silver pastes using MO technology and resin reinforcing technology, in: *2014 International Conference on Electronics Packaging (ICEP)*, 2014, pp. 526–531.
- [13] M. Fathidoost, Y. Yang, M. Oechsner, B.-X. Xu, Data-driven thermal and percolation analyses of 3D composite structures with interface resistance, *Mater. Des.* 227 (2023) 111746, <https://doi.org/10.1016/j.matdes.2023.111746>, <https://linkinghub.elsevier.com/retrieve/pii/S0264127523001612>.
- [14] B. Shi, L. Dong, M. Li, B. Liu, K. Kim, X. Xu, J. Zhou, J. Liu, Thermal percolation in composite materials with electrically conductive fillers, *Appl. Phys. Lett.* 113 (4) (2018) 041902, <https://doi.org/10.1063/1.5039923>, <http://aip.scitation.org/doi/10.1063/1.5039923>.
- [15] J. Zhong, Q. Xi, J. He, J. Liu, J. Zhou, Thermal percolation and electrical insulation in composite materials with partially metallic coated fillers, arXiv:2109.09921 [physics], Sep. 2021, <http://arxiv.org/abs/2109.09921>.
- [16] H. Bao, J. Chen, X. Gu, B. Cao, A Review of Simulation Methods in Micro/Nanoscale Heat Conduction, *ES Energy & Environment*, 2018, <http://www.espublisher.com/journals/articledetails/60/>.
- [17] I.Y. Forero-Sandoval, A.P. Franco-Bacca, F. Cervantes-Álvarez, C.L. Gómez-Heredia, J.A. Ramírez-Rincón, J. Ordóñez-Miranda, J.J. Alvarado-Gil, Electrical and thermal percolation in two-phase materials: a perspective, *J. Appl. Phys.* 131 (23) (2022) 230901, <https://doi.org/10.1063/5.0091291>, <https://aip.scitation.org/doi/10.1063/5.0091291>.
- [18] F. Qin, Y. Hu, Y. Dai, T. An, P. Chen, Evaluation of thermal conductivity for sintered silver considering aging effect with microstructure based model, *Microelectron. Reliab.* 108 (2020) 113633, <https://doi.org/10.1016/j.microrel.2020.113633>, <http://www.sciencedirect.com/science/article/pii/S0026271419310303>.
- [19] F. Qin, Y. Hu, Y. Dai, T. An, P. Chen, Y. Gong, H. Yu, Crack effect on the equivalent thermal conductivity of porously sintered silver, *J. Electron. Mater.* 49 (10) (2020) 5994–6008, <https://doi.org/10.1007/s11664-020-08325-1>.
- [20] J. Ordóñez-Miranda, M. Hermens, I. Nikitina, V.G. Kouznetsova, O. van der Sluis, M.A. Ras, J. Reparaz, M. Wagner, M. Sledzinska, J. Gomis-Bresco, C. Sotomayor Torres, B. Wunderle, S. Volz, Measurement and modeling of the effective thermal conductivity of sintered silver pastes, *Int. J. Therm. Sci.* 108 (2016) 185–194, <https://doi.org/10.1016/j.ijthermalsci.2016.05.014>, <https://linkinghub.elsevier.com/retrieve/pii/S1290072915302805>.
- [21] C. Du, G. Zou, B. Feng, J. Huo, Z. A. Y. Xiao, W. Wang, L. Liu, Predicting effective thermal conductivity of sintered silver by microstructural-simulation-based machine learning, *J. Electron. Mater.* (Jan. 2023), <https://doi.org/10.1007/s11664-022-10172-1>.
- [22] C. Gabbett, L. Doolan, K. Synnatschke, L. Gambini, E. Coleman, A.G. Kelly, S. Liu, E. Caffrey, J. Munuera, C. Murphy, S. Sanvito, L. Jones, J.N. Coleman, Quantitative analysis of printed nanostructured networks using high-resolution 3D FIB-SEM nanotomography, *Nat. Commun.* 15 (1) (2024) 278, <https://doi.org/10.1038/s41467-023-44450-1>, <https://www.nature.com/articles/s41467-023-44450-1>.
- [23] M. Groeber, B. Haley, M. Uchic, D. Dimiduk, S. Ghosh, 3D reconstruction and characterization of polycrystalline microstructures using a FIB-SEM system, *Mater. Charact.* 57 (4–5) (2006) 259–273, <https://doi.org/10.1016/j.matchar.2006.01.019>, <https://linkinghub.elsevier.com/retrieve/pii/S1044580306000623>.
- [24] W. Rmilid, N. Vivet, S. Chupin, T. Le Bihan, G. Le Quilliec, C. Richard, Quantitative analysis of porosity and transport properties by FIB-SEM 3D imaging of a solder based sintered silver for a new microelectronic component, *J. Electron. Mater.* 45 (4) (2016) 2242–2251.
- [25] K.K. Bodla, J.Y. Murthy, S.V. Garimella, Direct simulation of thermal transport through sintered Wick microstructures, *J. Heat Transf.* 134 (Nov. 2011) 012602, <https://doi.org/10.1115/1.4004804>.
- [26] K.H. N'Tsouaglo, X. Milhet, J. Colin, L. Signor, A. Nait-Ali, J. Creus, M. Gueguen, P. Gadaud, M. Legros, Time resolved evolution of the 3D nanoporous structure of sintered Ag by X-ray nanotomography: role of the interface with a copper substrate, *Adv. Eng. Mater.* (2021), <https://doi.org/10.1002/adem.202100583>, <https://onlinelibrary.wiley.com/doi/10.1002/adem.202100583>.
- [27] M. Song, G. Zhou, N. Lu, J. Lee, E. Nakouzi, H. Wang, D. Li, Oriented attachment induces fivefold twins by forming and decomposing high-energy grain boundaries, *Science* 367 (6473) (2020) 40–45, <https://doi.org/10.1126/science.aax6511>, <https://www.science.org/doi/10.1126/science.aax6511>.
- [28] K. Pietrak, T.S. Wisniewski, A review of models for effective thermal conductivity of composite materials, 2015, p. 11.
- [29] J.C. Ferguson, F. Semeraro, J.M. Thornton, F. Panerai, A. Borner, N.N. Mansour, Update 3.0 to “PuMA: the porous microstructure analysis software”, (PII:S2352711018300281), *SoftwareX* 15 (2021) 100775, <https://doi.org/10.1016/j.softx.2021.100775>, <https://linkinghub.elsevier.com/retrieve/pii/S235271102100090X>.
- [30] D.G. Cahill, W.K. Ford, K.E. Goodson, G.D. Mahan, A. Majumdar, H.J. Maris, R. Merlin, S.R. Phillpot, Nanoscale thermal transport, *Journal of Applied Physics* 93 (2) (2002) 793–818, <https://doi.org/10.1063/1.1524305>, publisher: American Institute of Physics, <https://aip.scitation.org/doi/10.1063/1.1524305>.
- [31] R.J. Warzoha, A.A. Wilson, B.F. Donovan, N. Donmezer, A. Giri, P.E. Hopkins, S. Choi, D. Pahinkar, J. Shi, S. Graham, Z. Tian, L. Ruppalt, Applications and impacts of nanoscale thermal transport in electronics packaging, *J. Electron. Packag.* 143 (2) (2021) 020804, <https://doi.org/10.1115/1.4049293>, <https://asmedigitalcollection.asme.org/electronicpackaging/article/143/2/020804/1091974/Applications-and-Impacts-of-Nanoscale-Thermal>.
- [32] D. Zhao, X. Qian, X. Gu, S.A. Jajja, R. Yang, Measurement techniques for thermal conductivity and interfacial thermal conductance of bulk and thin film materials, *J. Electron. Packag.* 138 (4) (2016) 040802.
- [33] Y. Xian, P. Zhang, S. Zhai, P. Yuan, D. Yang, Experimental characterization methods for thermal contact resistance: a review, *Appl. Therm. Eng.* 130 (2018) 1530–1548, <https://doi.org/10.1016/j.applthermaleng.2017.10.163>, <https://linkinghub.elsevier.com/retrieve/pii/S1359431117301291>.
- [34] W.J. Parker, R.J. Jenkins, C.P. Butler, G.L. Abbott, Flash method of determining thermal diffusivity, heat capacity, and thermal conductivity, *J. Appl. Phys.* 32 (9) (1961) 1679–1684, <https://doi.org/10.1063/1.1728417>, publisher: American Institute of Physics, <https://aip.scitation.org/doi/10.1063/1.1728417>.
- [35] L.N. Acquaroli, 3-omega method for thermal properties of thin film multilayers, arXiv:1811.00571 [cond-mat], Nov. 2018, <http://arxiv.org/abs/1811.00571>.
- [36] J. Standard, JESD51-14 - transient dual interface test method for the measurement of the thermal resistance junction-to-case of semiconductor devices with heat flow through a single path, Tech. rep., JEDEC, 2010, <https://www.jedec.org/standards-documents/docs/jesd51-14-0>.
- [37] H.A. Martin, E.C.P. Smits, R.H. Poelma, W.D. van Driel, G. Zhang, Online condition monitoring methodology for power electronics package reliability assessment, *IEEE Trans. Power Electron.* (2024) 1–10, <https://doi.org/10.1109/TPEL.2024.3352747>.
- [38] A. Cecen, H. Dai, Y.C. Yabansu, S.R. Kalidindi, L. Song, Material structure-property linkages using three-dimensional convolutional neural networks, *Acta Mater.* 146 (2018) 76–84, <https://doi.org/10.1016/j.actamat.2017.11.053>, <https://www.sciencedirect.com/science/article/pii/S1359645417310443>.
- [39] B.S. Fromm, K. Chang, D.L. McDowell, L.-Q. Chen, H. Garmestani, Linking phase-field and finite-element modeling for process-structure-property relations of a Ni-base superalloy, *Acta Mater.* 60 (17) (2012) 5984–5999, <https://doi.org/10.1016/j.actamat.2012.06.058>, <https://linkinghub.elsevier.com/retrieve/pii/S1359645412004302>.
- [40] D. Şöpu, C. Soyarslan, B. Sarac, S. Bargmann, M. Stoica, J. Eckert, Structure-property relationships in nanoporous metallic glasses, *Acta Mater.* 106 (2016) 199–207, <https://doi.org/10.1016/j.actamat.2015.12.026>, <https://linkinghub.elsevier.com/retrieve/pii/S135964541530135X>.
- [41] A. Gillman, M.J.G.H. Roelofs, K. Matouš, V.G. Kouznetsova, O. van der Sluis, M.P.F.H.L. van Maris, Microstructure statistics–property relations of silver particle-based interconnects, *Mater. Des.* 118 (2017) 304–313, <https://doi.org/10.1016/j.matdes.2017.01.005>, <https://www.sciencedirect.com/science/article/pii/S0264127517300059>.
- [42] T.F. Scientific, Software for electron microscopes: auto slice view software, URL, <https://www.thermofisher.com/nl/en/home/electron-microscopy/products/software-em-3d-vis/auto-slice-view-4-software.html>. (Accessed 26 January 2024).
- [43] T.F. Scientific, Software for ct and microscopy image data visualization and analysis: Avizo software, URL, <https://www.thermofisher.com/nl/en/home/electron-microscopy/products/software-em-3d-vis/avizo-software.html>. (Accessed 26 January 2024).

- [44] J. Fu, H.R. Thomas, C. Li, Tortuosity of porous media: image analysis and physical simulation, *Earth-Sci. Rev.* 212 (2021) 103439.
- [45] R.I. Al-Raoush, I.T. Madhoun, TORT3D: a MATLAB code to compute geometric tortuosity from 3D images of unconsolidated porous media, *Powder Technol.* 320 (2017) 99–107, <https://doi.org/10.1016/j.powtec.2017.06.066>, <https://www.sciencedirect.com/science/article/pii/S0032591017305375>.
- [46] J.A. Taillon, C. Pellegrinelli, Y.-L. Huang, E.D. Wachsman, L.G. Salamanca-Riba, Improving microstructural quantification in FIB/SEM nanotomography, *Ultramicroscopy* 184 (2018) 24–38, <https://doi.org/10.1016/j.ultramic.2017.07.017>, <https://www.sciencedirect.com/science/article/pii/S0304399116302261>.
- [47] D. Kim, S. Nagao, C. Chen, N. Wakasugi, Y. Yamamoto, A. Suetake, T. Takemasa, T. Sugahara, K. Sukanuma, Online thermal resistance and reliability characteristic monitoring of power modules with Ag sinter joining and Pb, Pb-free solders during power cycling test by SiC teg chip, *IEEE Trans. Power Electron.* 36 (5) (2021) 4977–4990.
- [48] V. Székely, T. Van Bien, Fine structure of heat flow path in semiconductor devices: a measurement and identification method, *Solid-State Electron.* 31 (9) (1988) 1363–1368.
- [49] V. Székely, A new evaluation method of thermal transient measurement results, in: *Thermal Investigations of ICs and Microstructures*, *Microelectron. J.* 28 (3) (1997) 277–292.
- [50] M. Rencz, V. Székely, A. Morelli, C. Villa, Determining partial thermal resistances with transient measurements, and using the method to detect die attach discontinuities, in: *Eighteenth Annual IEEE Semiconductor Thermal Measurement and Management Symposium*, Proceedings 2002 (Cat. No. 02CH37311), 2002, pp. 15–20.
- [51] A. Sghuri, Y. Billaud, L. Signor, D. Saury, X. Milhet, Experimental investigation of thermal conductivity during aging of nanoporous sintered silver, *Acta Mater.* (2023) 119109, <https://doi.org/10.1016/j.actamat.2023.119109>, <https://www.sciencedirect.com/science/article/pii/S1359645423004408>.
- [52] Delft High Performance Computing Centre (DHPC), DelftBlue supercomputer (phase 1), <https://www.tudelft.nl/dhpc/ark:/44463/DelftBluePhase1>, 2022.
- [53] X. Wu, L. Sun, Y. Liu, Z. Ye, X. Zhao, Y. Liu, Preparation and performance of Sn-based composite solder joints by solid-liquid low-temperature solder bonding technology, *J. Mater. Res. Technol.* 24 (2023) 6378–6390, <https://doi.org/10.1016/j.jmrt.2023.04.234>, <https://www.sciencedirect.com/science/article/pii/S2238785423009298>.
- [54] Y. Chen, Z. He, Z. Zhang, M. Yang, R. An, Mechanical property and void ratio of several Pb-containing and Pb-free solder joints in space power electronics, in: *2014 15th International Conference on Electronic Packaging Technology*, 2014, pp. 340–342, <https://ieeexplore.ieee.org/document/6922668>.
- [55] S. Gong, G. Chen, S. Qu, A. Ren, V. Duk, Q. Shi, G. Zhang, Shear strength and fracture analysis of Sn-9Zn-2.5Bi-1.5In and Sn-3.0Ag-0.5Cu pastes with Cu-substrate joints under different reflow times, *Microelectron. Reliab.* 127 (2021) 114378, <https://doi.org/10.1016/j.microrel.2021.114378>, <https://www.sciencedirect.com/science/article/pii/S0026271421003449>.
- [56] R. Kolenak, A. Pluhar, J. Drapala, P. Gogola, M. Pasak, M. Sloboda, Characterization of an active soldering Zn-Mg alloy and the study of ultrasonic soldering of SiC ceramics with copper substrate, *Appl. Sci.* 14 (4) (2024) 1504, <https://doi.org/10.3390/app14041504>, Publisher: Multidisciplinary Digital Publishing Institute, <https://www.mdpi.com/2076-3417/14/4/1504>.
- [57] L. Yin, F. Yang, X. Bao, W. Xue, Z. Du, X. Wang, J. Cheng, H. Ji, J. Sui, X. Liu, Y. Wang, F. Cao, J. Mao, M. Li, Z. Ren, Q. Zhang, Low-temperature sintering of Ag nanoparticles for high-performance thermoelectric module design, *Nat. Energy* 8 (7) (2023) 665–674, <https://doi.org/10.1038/s41560-023-01245-4>, publisher: Nature Publishing Group, <https://www.nature.com/articles/s41560-023-01245-4>.
- [58] G. Qu, Z. Deng, W. Guo, Z. Peng, Q. Jia, E. Deng, H. Zhang, The heat-dissipation sintered interface of power chip and heat sink and its high-temperature thermal analysis, in: *IEEE Transactions on Components, Packaging and Manufacturing Technology*, *IEEE Trans. Compon. Packag. Manuf. Technol.* 13 (6) (2023) 816–822, <https://doi.org/10.1109/TCPMT.2023.3290303>, <https://ieeexplore.ieee.org/document/10167667>.
- [59] J.G. Bai, Z.Z. Zhang, J.N. Calata, G.-q. Lu, Characterization of low-temperature sintered nanoscale silver paste for attaching semiconductor devices, in: *2005 Conference on High Density Microsystem Design and Packaging and Component Failure Analysis*, 2005, pp. 1–5, <https://ieeexplore.ieee.org/document/4017453>.
- [60] Z. Zhang, G.-Q. Lu, Pressure-assisted low-temperature sintering of silver paste as an alternative die-attach solution to solder reflow, in: *IEEE Transactions on Electronics Packaging Manufacturing*, *IEEE Trans. Electron. Packag. Manuf.* 25 (4) (2002) 279–283, <https://doi.org/10.1109/TEPM.2002.807719>, <https://ieeexplore.ieee.org/document/1176910>.
- [61] Y. Wu, G. Zou, S. Wang, W. Guo, H. Zhang, L. Liu, Interfacial bonding mechanisms of sintered Cu nanoparticles on different metallization surfaces, *Surf. Interfaces* 46 (2024) 104173, <https://doi.org/10.1016/j.surfint.2024.104173>, <https://linkinghub.elsevier.com/retrieve/pii/S2468023024003328>.
- [62] J. Kahler, N. Heuck, A. Wagner, A. Stranz, E. Peiner, A. Waag, Sintering of copper particles for die attach, in: *IEEE Transactions on Components, Packaging and Manufacturing Technology*, *IEEE Trans. Compon. Packag. Manuf. Technol.* 2 (10) (2012) 1587–1591, <https://doi.org/10.1109/TCPMT.2012.2201940>, <https://ieeexplore.ieee.org/document/6236102>.
- [63] X. Wang, H. Chen, Z. Yang, W. Liu, Z. Zeng, G. Zhang, J. Zhang, J. Fan, P. Liu, Microstructure evolution and micromechanical behavior of solvent-modified Cu–Ag composite sintered joints for power electronics packaging at high temperatures, *J. Mater. Res. Technol.* 30 (2024) 8433–8450, <https://doi.org/10.1016/j.jmrt.2024.05.196>, <https://www.sciencedirect.com/science/article/pii/S2238785424012365>.
- [64] Y. Liu, C. Chen, Y. Wang, Z. Zhang, R. Liu, M. Ueshima, I. Ota, H. Nishikawa, M. Nishijima, K.S. Nakayama, K. Sukanuma, Development of Ag@Si composite sinter joining with ultra-high resistance to thermal shock test for SiC power device: experiment validation and numerical simulation, *Composites, Part B, Eng.* 281 (2024) 111519, <https://doi.org/10.1016/j.compositesb.2024.111519>, <https://www.sciencedirect.com/science/article/pii/S1359836824003305>.
- [65] J. Wang, S. Yodo, H. Tatsumi, H. Nishikawa, Reliability-enhanced microscale Ag sintered joint doped with AlN nanoparticles, *Mater. Lett.* 349 (2023) 134845, <https://doi.org/10.1016/j.matlet.2023.134845>, <https://www.sciencedirect.com/science/article/pii/S0167577X23010303>.
- [66] S. Gao, Z. Yang, Y. Tan, X. Li, X. Chen, Z. Sun, G.-Q. Lu, Bonding of large substrates by silver sintering and characterization of the interface thermal resistance, in: *IEEE Transactions on Industry Applications*, *IEEE Trans. Ind. Appl.* 55 (2) (2019) 1828–1834, <https://doi.org/10.1109/TIA.2018.2879957>, <https://ieeexplore.ieee.org/abstract/document/8526336>.
- [67] R. Sattari, D. Hu, X. Liu, H. van Zeijl, S. Vollebregt, G. Zhang, Transient thermal measurement on nano-metallic sintered die-attach joints using a thermal test chip, *Appl. Therm. Eng.* 221 (2023) 119503, <https://doi.org/10.1016/j.applthermaleng.2022.119503>, <https://www.sciencedirect.com/science/article/pii/S1359431122014338>.
- [68] K. Murayama, H. Ota, K. Oi, Thermal characteristic evaluation of silver and copper sintering materials, in: *2019 IEEE 21st Electronics Packaging Technology Conference (EPTC)*, 2019, pp. 300–304, <https://ieeexplore.ieee.org/abstract/document/9026702>.
- [69] Y. Wu, G. Zou, S. Wang, W. Guo, H. Zhang, P. Peng, B. Feng, L. Liu, Rapid and low temperature sintering bonding using Cu nanoparticle film for power electronic packaging, *Appl. Surf. Sci.* 603 (2022) 154422, <https://doi.org/10.1016/j.apsusc.2022.154422>, <https://www.sciencedirect.com/science/article/pii/S016943322019559>.